A comparison of two Kalman-type filters for robust extrapolation of offshore wind turbine support structure response

Tatsis, K.; Lourens, Eliz-Mari

DOI
10.1201/9781315375175-25

Publication date
2016

Document Version
Accepted author manuscript

Published in
Life-Cycle of Engineering Systems: Emphasis on Sustainable Civil Infrastructure

IALCCE 2016: Fifth International Symposium on Life-Cycle Civil Engineering
October 16-19, 2016 / The Netherlands, Delft

A comparison of two Kalman-type filters for robust extrapolation of offshore wind turbine support structure response

K. Tatsis & E. Lourens
Faculty of Civil Engineering and Geosciences, Delft University of Technology, Delft, The Netherlands

ABSTRACT: Quasi-periodic loading resulting from waves and a rotationally sampled wind field often leads to fatigue-driven designs for offshore wind turbine support structures. The uncertainty on wind and wave loading, together with large modelling uncertainties, lead to large discrepancies between the observed and predicted dynamic behaviour of these structures. Among many recent-developed techniques for monitoring of true fatigue damage development, two promising Kalman-type filters are compared, namely the recently proposed Dual Kalman filter (DKF) and the Gillijns and De Moor filter (GDF). The filters are applied to synthetic vibration data in order to predict the global response of a lattice support structure assuming large modelling uncertainties and no knowledge of the input forces. A critical assessment of both filters with regard to requirements on the available data and tuning of the filter parameters is presented.

1 INTRODUCTION

With strict targets in place for the reduction of the levelized cost-of-energy of offshore wind, a diverse range of possible cost reduction schemes is being investigated. Among them are the life-time extension of offshore wind turbines/farms, and the accompanying investigation into the fatigue life of offshore wind support structures. Fatigue life predictions are based on processed historical metocean data applied to a numerical model of the offshore turbine in aeroelastic simulations where different operating conditions are taken into account.

The true accumulated fatigue damage during the operating life of the turbine will differ from the predicted damage due to metocean conditions deviating from those assumed, errors in the numerical model (e.g. foundation stiffness), various turbine faults (e.g. blade pitch errors), etc. There is thus a need for monitoring systems capable of tracking accumulated fatigue damage at all critical locations in a support structure based on actual observations. Since the critical locations are mostly located underneath the water line, some form of downward extrapolation of the response measured above the sea level is required. Given that the first natural frequency of installed turbines can deviate from the design value with up to 10%, it is not sufficient to base this extrapolation on the numerical model only.

Instead, algorithms capable of jointly estimating the states (displacements/velocities) and input forces can be used. Response prediction on the basis of jointly estimated states and input was first proposed in Lourens, Papadimitriou, Gillijns, Reynders, de Roeck, & Lombaert 2012, where additionally it was shown that the identification of a set of (equivalent) forces can to some extent compensate for inaccuracies in the extrapolated response due to modeling errors. The concept was later applied to an offshore wind turbine lattice support structure by Van der Male & Lourens (2015), where the capability to compensate for modelling errors was again illustrated using a numerical example.

The algorithm used in Van der Male & Lourens (2015) suffers, however, from an important drawback, namely that the state estimates are affected by spurious low-frequency components in situations where displacement and/or strain data are not available. A number of related methods has since been suggested, one of them being the Dual Kalman filter (Azam, Chatzi, & Papadimitriou 2015). For a state-of-the-art review, the reader is referred to Azam, Chatzi, Papadimitriou, & Smyth 2015.

In this contribution, a comparison is made between two of those promising Kalman-type filters capable of robustly extrapolating the response of a wind turbine support structure. Synthetic measurement data is generated by applying aero- and hydrodynamic loading to an offshore wind turbine supported on a lattice support structure. The response extrapolation is performed assuming large modelling uncertainties and no prior knowledge of the input forces. Finally, a critical assessment of both filters is presented, with the focus on tuning of the filter parameters and requirements on the available data.

2 MATHEMATICAL FORMULATION

The continuous-time equations of motion for a space-discretized linear system are written as:

$$\mathbf{M}\ddot{\mathbf{u}}(t) + \mathbf{C}\dot{\mathbf{u}}(t) + \mathbf{K}\mathbf{u}(t) = \mathbf{S}_{\mathrm{p}}\,\mathbf{p}(t) \tag{1}$$

where $\mathbf{u}(t) \in \mathbb{R}^{n_{\mathrm{dof}}}$ is the displacement vector and $\mathbf{M}$, $\mathbf{C}$ and $\mathbf{K} \in \mathbb{R}^{n_{\mathrm{dof}} \times n_{\mathrm{dof}}}$ are the mass, damping and stiffness matrices, respectively. The excitation vector on the right-hand side is factorized into the force selection matrix $\mathbf{S}_{\mathrm{p}} \in \mathbb{R}^{n_{\mathrm{dof}} \times n_{\mathrm{p}}}$ and the input force vector $\mathbf{p}(t) \in \mathbb{R}^{n_{\mathrm{p}}}$ with n_{p} denoting the number of input forces.

Upon introduction of the coordinate transformation $\mathbf{u}(t) = \mathbf{\Phi}\mathbf{z}(t)$ and premultiplication by $\mathbf{\Phi}^{\mathrm{T}}$, the equation of motion is transformed to:

$$\ddot{\mathbf{z}}(t) + \mathbf{\Gamma}\dot{\mathbf{z}}(t) + \mathbf{\Omega}^2\mathbf{z}(t) = \mathbf{\Phi}^{\mathrm{T}}\mathbf{S}_{\mathrm{p}}\,\mathbf{p}(t) \tag{2}$$

in which $\mathbf{z}(t) \in \mathbb{R}^{n_{\mathrm{m}}}$ represents the vector of modal coordinates and $\mathbf{\Phi} \in \mathbb{R}^{n_{\mathrm{dof}} \times n_{\mathrm{m}}}$ contains the mass-normalized mode shapes. The diagonal matrix $\mathbf{\Omega} \in \mathbb{R}^{n_{\mathrm{m}} \times n_{\mathrm{m}}}$ contains the natural frequencies ω_i and the modal damping matrix $\mathbf{\Gamma} \in \mathbb{R}^{n_{\mathrm{m}} \times n_{\mathrm{m}}}$, which is also diagonal, collects the terms $2\xi_i\omega_i$ with ξ denoting the modal damping ratio.

Introducing now the state vector $\mathbf{x}(t) \in \mathbb{R}^{n_{\mathrm{s}} \times n_{\mathrm{s}}}$, where $\mathbf{x}(t) = [\,\mathbf{u}(t)\;\; \dot{\mathbf{u}}(t)\,]^{\mathrm{T}}$ and $n_{\mathrm{s}} = 2n_{\mathrm{dof}}$, Eq. (1) can be rewritten in the following form:

$$\dot{\mathbf{x}}(t) = \mathbf{A}_{\mathrm{c}}\,\mathbf{x}(t) + \mathbf{B}_{\mathrm{c}}\,\mathbf{p}(t) \tag{3}$$

where the system matrices $\mathbf{A}_{\mathrm{c}} \in \mathbb{R}^{n_{\mathrm{s}} \times n_{\mathrm{s}}}$ and $\mathbf{B}_{\mathrm{c}} \in \mathbb{R}^{n_{\mathrm{s}} \times n_{\mathrm{p}}}$ are defined as:

$$\mathbf{A}_{\mathrm{c}} = \begin{bmatrix} \mathbf{0} & \mathbf{I} \\ -\mathbf{M}^{-1}\mathbf{K} & -\mathbf{M}^{-1}\mathbf{C} \end{bmatrix}, \quad \mathbf{B}_{\mathrm{c}} = \begin{bmatrix} \mathbf{0} \\ \mathbf{M}^{-1}\mathbf{S}_{\mathrm{p}} \end{bmatrix}$$

The measurement vector $\mathbf{d}(t) \in \mathbb{R}^{n_{\mathrm{d}}}$, with n_{d} the number of measured quantities, reads

$$\mathbf{d}(t) = \begin{bmatrix} \mathbf{S}_{\mathrm{d,d}} & \mathbf{0} & \mathbf{0} \\ \mathbf{0} & \mathbf{S}_{\mathrm{d,v}} & \mathbf{0} \\ \mathbf{0} & \mathbf{0} & \mathbf{S}_{\mathrm{d,a}} \end{bmatrix} \begin{bmatrix} \mathbf{u}(t) \\ \dot{\mathbf{u}}(t) \\ \ddot{\mathbf{u}}(t) \end{bmatrix} \tag{4}$$

where $\mathbf{S}_{\mathrm{d,d}}$, $\mathbf{S}_{\mathrm{d,v}}$ and $\mathbf{S}_{\mathrm{d,a}}$ are the selection matrices for displacements, velocities and accelerations respectively. Making use of the equation of motion and the definition of the state vector $\mathbf{x}(t)$, the measurement vector can be rewritten into state-space form:

$$\mathbf{d}(t) = \mathbf{G}_{\mathrm{c}}\,\mathbf{x}(t) + \mathbf{J}_{\mathrm{c}}\,\mathbf{p}(t) \tag{5}$$

where the output influence matrix $\mathbf{G}_{\mathrm{c}} \in \mathbb{R}^{n_{\mathrm{d}} \times n_{\mathrm{s}}}$ and the direct transmission matrix $\mathbf{J}_{\mathrm{c}} \in \mathbb{R}^{n_{\mathrm{d}} \times n_{\mathrm{p}}}$ are defined as:

$$\mathbf{G}_{\mathrm{c}} = \begin{bmatrix} \mathbf{S}_{\mathrm{d,d}} & \mathbf{0} \\ \mathbf{0} & \mathbf{S}_{\mathrm{d,v}} \\ \mathbf{S}_{\mathrm{d,a}}\mathbf{M}^{-1}\mathbf{K} & \mathbf{S}_{\mathrm{d,a}}\mathbf{M}^{-1}\mathbf{C} \end{bmatrix}, \; \mathbf{J}_{\mathrm{c}} = \begin{bmatrix} \mathbf{0} \\ \mathbf{0} \\ \mathbf{S}_{\mathrm{d,a}}\mathbf{M}^{-1}\mathbf{S}_{\mathrm{p}} \end{bmatrix}$$

Eqs. (3) and (5) together constitute the full-order state-space equations in the continuous-time domain. In the case of a reduced order model, the dynamics of the system may be represented by a reduced number n_{m} of modal coordinates $\mathbf{z}(t)$, so that the state vector can be written as

$$\mathbf{x}(t) = \begin{bmatrix} \mathbf{\Phi} & \mathbf{0} \\ \mathbf{0} & \mathbf{\Phi} \end{bmatrix} \boldsymbol{\zeta}(t) \tag{6}$$

in which $\boldsymbol{\zeta}(t) \in \mathbb{R}^{2n_{\mathrm{m}}}$ is the modal state vector: $\boldsymbol{\zeta}(t) = [\,\mathbf{z}(t)\;\; \dot{\mathbf{z}}(t)\,]^{\mathrm{T}}$. Accordingly, the full order state-space model is transformed to the modal state-space model of reduced order:

$$\dot{\boldsymbol{\zeta}}(t) = \mathbf{A}_{\mathrm{c}}\,\boldsymbol{\zeta}(t) + \mathbf{B}_{\mathrm{c}}\,\mathbf{p}(t) \tag{7}$$

$$\mathbf{d}(t) = \mathbf{G}_{\mathrm{c}}\,\boldsymbol{\zeta}(t) + \mathbf{J}_{\mathrm{c}}\,\mathbf{p}(t) \tag{8}$$

where the corresponding system matrices $\mathbf{A}_{\mathrm{c}} \in \mathbb{R}^{2n_{\mathrm{m}} \times 2n_{\mathrm{m}}}$, $\mathbf{B}_{\mathrm{c}} \in \mathbb{R}^{2n_{\mathrm{m}} \times n_{\mathrm{p}}}$, $\mathbf{G}_{\mathrm{c}} \in \mathbb{R}^{n_{\mathrm{d}} \times 2n_{\mathrm{m}}}$ and $\mathbf{J}_{\mathrm{c}} \in \mathbb{R}^{n_{\mathrm{d}} \times n_{\mathrm{p}}}$ are now defined as:

$$\mathbf{A}_{\mathrm{c}} = \begin{bmatrix} \mathbf{0} & \mathbf{I} \\ -\mathbf{\Omega}^2 & -\mathbf{\Gamma} \end{bmatrix}, \quad \mathbf{B}_{\mathrm{c}} = \begin{bmatrix} \mathbf{0} \\ \mathbf{\Phi}^{\mathrm{T}}\mathbf{S}_{\mathrm{p}} \end{bmatrix}$$

$$\mathbf{G}_{\mathrm{c}} = \begin{bmatrix} \mathbf{S}_{\mathrm{d,d}}\,\mathbf{\Phi} & \mathbf{0} \\ \mathbf{0} & \mathbf{S}_{\mathrm{d,v}}\,\mathbf{\Phi} \\ \mathbf{S}_{\mathrm{d,a}}\mathbf{\Phi}\,\mathbf{\Omega}^2 & \mathbf{S}_{\mathrm{d,a}}\mathbf{\Phi}\,\mathbf{\Gamma} \end{bmatrix}, \quad \mathbf{J}_{\mathrm{c}} = \begin{bmatrix} \mathbf{0} \\ \mathbf{0} \\ \mathbf{S}_{\mathrm{d,a}}\mathbf{\Phi}\mathbf{\Phi}^{\mathrm{T}}\mathbf{S}_{\mathrm{p}} \end{bmatrix}$$

The equivalent discrete-time state-space model is then obtained after discretization of Eqs. (7) and (8) with a sampling rate of $1/\Delta t$:

$$\boldsymbol{\zeta}_{k+1} = \mathbf{A}\,\boldsymbol{\zeta}_k + \mathbf{B}\,\mathbf{p}_k \tag{9}$$

$$\mathbf{d}_k = \mathbf{G}\,\boldsymbol{\zeta}_k + \mathbf{J}\,\mathbf{p}_k \tag{10}$$

where $\boldsymbol{\zeta}_k = \boldsymbol{\zeta}(k\Delta t)$, $\mathbf{p}_k = \mathbf{p}(k\Delta t)$, $\mathbf{d}_k = \mathbf{d}(k\Delta t)$ for $k = 1, ..., N_t$ and

$$\mathbf{A} = e^{\mathbf{A}_{\mathrm{c}}\Delta t}, \quad \mathbf{B} = [\mathbf{A} - \mathbf{I}]\,\mathbf{A}_{\mathrm{c}}^{-1}\mathbf{B}_{\mathrm{c}}, \quad \mathbf{G} = \mathbf{G}_{\mathrm{c}}, \quad \mathbf{J} = \mathbf{J}_{\mathrm{c}}.$$

3 JOINT INPUT-STATE ESTIMATION

Consider the discrete-time state-space equations supplemented with the random variables $\mathbf{w}_k^{\zeta} \in \mathbb{R}^{2n_{\mathrm{m}}}$ and $\mathbf{v}_k \in \mathbb{R}^{n_{\mathrm{d}}}$ respectively, in order to account for process (modelling) and measurement noise:

$$\boldsymbol{\zeta}_{k+1} = \mathbf{A}\,\boldsymbol{\zeta}_k + \mathbf{B}\,\mathbf{p}_k + \mathbf{w}_k^{\zeta} \tag{11}$$

$$\mathbf{d}_k = \mathbf{G}\boldsymbol{\zeta}_k + \mathbf{J}\mathbf{p}_k + \mathbf{v}_k \tag{12}$$

The noise processes are assumed to be mutually uncorrelated, zero-mean, white noise signals with known covariance matrices $\mathbf{Q}^{\zeta} = \mathbb{E}\left\{\mathbf{w}_k\,\mathbf{w}_l^{\mathrm{T}}\right\} \geq 0$ and $\mathbf{R} = \mathbb{E}\left\{\mathbf{v}_k\,\mathbf{v}_l^{\mathrm{T}}\right\} > 0$ for $k, l = 1, ..., N_t$ with zero off-diagonal entries. Assuming no knowledge of the driving forces, the problem at hand is to estimate the input $\mathbf{p}_k$ and the state $\boldsymbol{\zeta}_k$ of the above system, relying on the noisy observations $\mathbf{d}_k$. To this end, two Kalman-type filters are implemented, the Dual Kalman fiter (DKF) and the Gillijns and De Moor filter (GDF).

3.1 *Dual Kalman Filter*

Within the context of this first algorithm a dual implementation of the Kalman filter is performed for estimating both the states and the input of linear time-invariant systems. This is accomplished by introducing a fictitious process for the unknown input:

$$\mathbf{p}_{k+1} = \mathbf{p}_k + \mathbf{w}_k^{\mathrm{p}} \tag{13}$$

in which $\mathbf{w}_k^{\mathrm{p}}$ is a zero mean white Gaussian noise whose associated covariance matrix is denoted by $\mathbf{Q}^{\mathrm{p}}$. The joint input-state estimation is then enabled by combining the two processes represented by Eqs. (11)-(12) and Eq. (13) respectively, upon proper tuning of the noise covariances $\mathbf{Q}^{\zeta}$, $\mathbf{Q}^{\mathrm{p}}$, and $\mathbf{R}$ and initialization of the expected value and the covariance of the state and the input. The general scheme is summarized in Table 1.

Table 1: The general scheme for the DKF algorithm

Initialization at time t_0:

$$\hat{\mathbf{p}}_0 = \mathbb{E}[\mathbf{p}_0]$$

$$\mathbf{P}_0^{\mathrm{p}} = \mathbb{E}\left[(\mathbf{p}_0 - \hat{\mathbf{p}}_0)(\mathbf{p}_0 - \hat{\mathbf{p}}_0)^{\mathrm{T}}\right]$$

$$\hat{\boldsymbol{\zeta}}_0 = \mathbb{E}[\boldsymbol{\zeta}_0]$$

$$\mathbf{P}_0^{\zeta} = \mathbb{E}\left[\left(\boldsymbol{\zeta}_0 - \hat{\boldsymbol{\zeta}}_0\right)\left(\boldsymbol{\zeta}_0 - \hat{\boldsymbol{\zeta}}_0\right)^{\mathrm{T}}\right]$$

At time t_k, for $k = 1, ..., N_t$:

- Input prediction

$$\mathbf{p}_k^- = \mathbf{p}_{k-1}$$

$$\mathbf{P}_k^{\mathrm{p}-} = \mathbf{P}_{k-1}^{\mathrm{p}} + \mathbf{Q}^{\mathrm{p}}$$

- Input update

$$\mathbf{K}_k^{\mathrm{p}} = \mathbf{P}_k^{\mathrm{p}-}\mathbf{J}^{\mathrm{T}}\left(\mathbf{J}\mathbf{P}_k^{\mathrm{p}-}\mathbf{J}^{\mathrm{T}} + \mathbf{R}\right)^{-1}$$

$$\hat{\mathbf{p}}_k = \mathbf{p}_k^- + \mathbf{K}_k^{\mathrm{p}}\left(\mathbf{d}_k - \mathbf{G}\hat{\boldsymbol{\zeta}}_{k-1} - \mathbf{J}\mathbf{p}_k^-\right)$$

$$\mathbf{P}_k^{\mathrm{p}} = \mathbf{P}_k^{\mathrm{p}-} - \mathbf{K}_k^{\mathrm{p}}\mathbf{J}\mathbf{P}_k^{\mathrm{p}-}$$

- State prediction

$$\boldsymbol{\zeta}_k^- = \mathbf{A}\hat{\boldsymbol{\zeta}}_{k-1} + \mathbf{B}\hat{\mathbf{p}}_k$$

$$\mathbf{P}_k^{\zeta-} = \mathbf{A}\mathbf{P}_{k-1}^{\zeta}\mathbf{A}^{\mathrm{T}} + \mathbf{Q}^{\zeta}$$

- State update

$$\mathbf{K}_k^{\zeta} = \mathbf{P}_k^{\zeta-}\mathbf{G}^{\mathrm{T}}\left(\mathbf{G}\mathbf{P}_k^{\zeta-}\mathbf{G}^{\mathrm{T}} + \mathbf{R}\right)^{-1}$$

$$\hat{\boldsymbol{\zeta}}_k = \boldsymbol{\zeta}_k^- + \mathbf{K}_k^{\zeta}\left(\mathbf{d}_k - \mathbf{G}\boldsymbol{\zeta}_k^- - \mathbf{J}\hat{\mathbf{p}}_k\right)$$

$$\mathbf{P}_k^{\zeta} = \mathbf{P}_k^{\zeta-} - \mathbf{K}_k^{\zeta}\mathbf{G}\mathbf{P}_k^{\zeta-}$$

3.2 *Gillijns and De Moor Filter*

The second algorithm to be assessed is the GDF, developed by Gillijns & De Moor 2007. Unlike the DKF, the GDF does not require any assumption on the input, and it is merely initialized using the initial state $\boldsymbol{\zeta}_0$ and its variance $\mathbf{P}_0^{\zeta}$. Analogous to the DKF, the covariances $\mathbf{Q}^{\zeta}$ and $\mathbf{R}$, of the process and measurement noise, respectively, must be properly chosen in order for the filter to furnish accurate estimates. Hereafter, the joint force and state estimation is done recursively in three steps: the input estimation, the measurement update and the time update. The general scheme of this algorithm is outlined in Table 2.

4 SIMULATED EXAMPLE

For the comparative study between the two algorithms, an offshore wind turbine support structure is considered, with properties as introduced by De Vries et al. (2011). The characteristics of the supported 5 MW reference turbine can be found in Jonkman et al. (2009). The entire structure is modelled with three-dimensional Euler-Bernoulli beam elements while the concrete transition piece between the

Table 2: The general scheme for the GDF algorithm

Initialization at time t_0:

$$\boldsymbol{\zeta}_0 = \mathbb{E}[\boldsymbol{\zeta}_0]$$

$$\mathbf{P}_0^{\zeta} = \mathbb{E}\left[\left(\boldsymbol{\zeta}_0 - \hat{\boldsymbol{\zeta}}_0\right)\left(\boldsymbol{\zeta}_0 - \hat{\boldsymbol{\zeta}}_0\right)^{\mathrm{T}}\right]$$

At time t_k, for $k = 1, ..., N_t$:

- Input prediction

$$\tilde{\mathbf{R}}_k = \mathbf{G}\mathbf{P}_k^{\zeta-}\mathbf{G}^{\mathrm{T}} + \mathbf{R}$$

$$\mathbf{M}_k = \left(\mathbf{J}^{\mathrm{T}}\tilde{\mathbf{R}}_k^{-1}\mathbf{J}\right)\mathbf{J}^{\mathrm{T}}\tilde{\mathbf{R}}_k^{-1}$$

$$\hat{\mathbf{p}}_k = \mathbf{M}_k\left(\mathbf{d}_k - \mathbf{G}\boldsymbol{\zeta}_k^-\right)$$

$$\mathbf{P}_k^{\mathrm{p}} = \left(\mathbf{J}^{\mathrm{T}}\tilde{\mathbf{R}}_k^{-1}\mathbf{J}\right)^{-1}$$

- Measurement update

$$\mathbf{L}_k = \mathbf{P}_k^{\zeta-}\mathbf{G}^{\mathrm{T}}\tilde{\mathbf{R}}_k^{-1}$$

$$\hat{\boldsymbol{\zeta}}_k = \hat{\boldsymbol{\zeta}}_k^- + \mathbf{L}_k\left(\mathbf{d}_k - \mathbf{G}\hat{\boldsymbol{\zeta}}_k^- - \mathbf{J}\hat{\mathbf{p}}_k\right)$$

$$\mathbf{P}_k^{\zeta} = \mathbf{P}_k^{\zeta-} - \mathbf{L}_k\left(\tilde{\mathbf{R}}_k - \mathbf{J}\mathbf{P}_k^{\mathrm{p}}\mathbf{J}^{\mathrm{T}}\right)\mathbf{L}_k^{\mathrm{T}}$$

$$\mathbf{P}_k^{\zeta\mathrm{p}} = \left(\mathbf{P}_k^{\mathrm{p}\zeta}\right)^{\mathrm{T}} = -\mathbf{L}_k\mathbf{J}\mathbf{P}_k^{\mathrm{p}}$$

- Time update

$$\hat{\boldsymbol{\zeta}}_{k+1}^- = \mathbf{A}\hat{\boldsymbol{\zeta}}_k + \mathbf{B}\hat{\mathbf{p}}_k$$

$$\mathbf{P}_{k+1}^{\zeta-} = [\mathbf{A} \quad \mathbf{B}]\begin{bmatrix}\mathbf{P}_k^{\zeta} & \mathbf{P}_k^{\zeta\mathrm{p}} \\ \mathbf{P}_k^{\mathrm{p}\zeta} & \mathbf{P}_k^{\mathrm{p}}\end{bmatrix}[\mathbf{A} \quad \mathbf{B}]^{\mathrm{T}} + \mathbf{Q}^{\zeta}$$

lattice structure and the tower is modelled as a rigid body. The rotor-nacelle assembly is reduced to a lumped mass on top of the tower and an additional point mass is placed in the middle of the tower in order to account for flanges, bolts and equipment installed in the tower. Soil-structure interaction is taken into account by means of vertically oriented linear spring elements at the base of the jacket legs whose stiffness is calibrated so that the first natural frequency of the model shows good agreement with that described by De Vries et al. (2011).

The implementation of the identification algorithms is based on a set of artificial vibration data generated by subjecting the full-order finite element model to a pair of environmental loads: a thrust force due to wind acting on the rotor disc and a wave load acting on the lattice structure.

For the modelling of the wind turbulence in the plane of the rotor disc, a von Karman wind spectrum is considered (Fig. 1):

$$S_{uu}(f) = \sigma_u^2 \frac{4L/\overline{U}}{\left(1 + 70.8\left(fL/\overline{U}\right)^2\right)^{5/6}}$$

where σ_u is the standard deviation of the turbulence velocity equal to 0.1, L is the isotropic integral length scale of wind turbulence equal to 150 m and $\overline{U}$ is the mean wind velocity chosen to be 12 m/s. The spatial variation of the wind speed seen by a rotating point on the blades of the wind turbine is taken into account by means of rotational

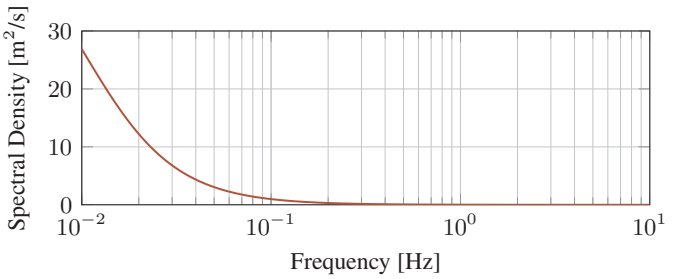

Figure 1: Von Karman wind spectrum for a mean wind speed of 12 m/s, turbulence intensity of 10% and turbulence length scale of 150 m

sampling of the wind field for a certain number, namely 10, of annular rings on the rotor disc, as elaborated by Burton et al. (2011). The resulting periodic excitation (Figure 2) exerted on the support structure is then obtained on the basis of the actuator disc concept (Burton, Jenkins, Sharpe, & Bossanyi 2011) and is assumed to act as a point load along the x-axis at the rotor nacelle assembly at the top of the tower. An 80 sec time frame of the obtained wind force is illustrated in Figure 5(a).

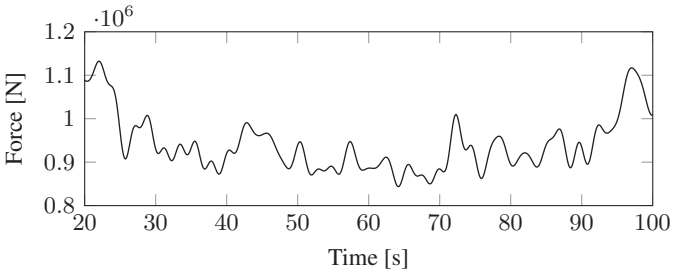

Figure 2: Aerodynamic force signal for NREL5 offshore wind turbine

The mean sea level in the examined location is assumed to be 50 m and the sea surface elevation is derived from a Pierson-Moskowitz spectrum (Fig. 3):

$$S_{hh}(f) = \alpha \frac{g^2}{(2\pi f)^5}\, e^{-\beta\left(\frac{g}{2\pi f \overline{U}}\right)^4}$$

The simulation is performed according to Shinozuka & Deodatis (1991) with an upper cut-off frequency of 3 Hz, for a mean wind speed $\overline{U}$ of 12 m/s and coefficients $\alpha = 0.0081$ and $\beta = 0.74$. Based on this distribution for the wave elevation, the water particle kinematics are determined using linear wave theory and the hydrodynamic loads on the members of the lattice structure are calculated with Morison's equation. The total wave force, for which a 80 sec

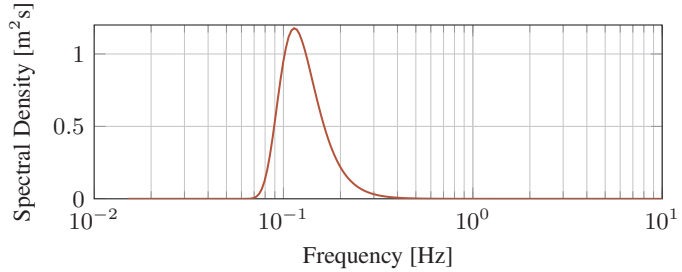

Figure 3: Pierson-Moskowitz wave spectrum for mean wind speed of 12 m/s

time frame is presented in Fig. 4, is assumed to act in the form of concentrated loads, along x-axis, on the legs of the jacket at the upper K-joints, as depicted in Fig. 5(a).

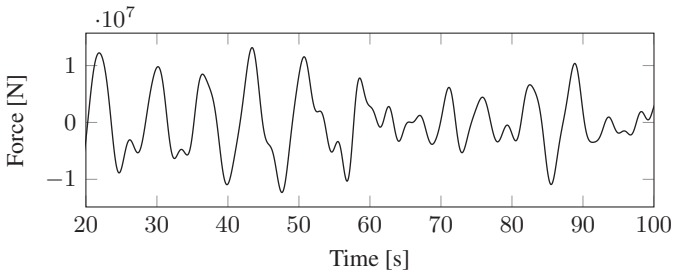

Figure 4: Hydrodynamic force signal on the jacket structure

Application of the force time signals on the finite element model at the positions presented in Fig. 5(a) yields the artificial measurement data, at the chosen sensor locations. Subsequently, the vector of measurement data $\mathbf{d}_k \in \mathbb{R}^{n_d}$ is polluted with Gaussian white noise, in order to generate the noisy output vector $\tilde{\mathbf{d}}_k \in \mathbb{R}^{n_d}$ at each time step k according to:

$$\tilde{\mathbf{d}}_k = \mathbf{d}_k + \delta\, \boldsymbol{\sigma}_d\, \mathbf{r}_k \tag{14}$$

where δ is the noise level, $\boldsymbol{\sigma}_d \in \mathbb{R}^{n_d \times n_d}$ is a diagonal matrix composed of the standard deviations of the measurement signals and $\mathbf{r}_k \in \mathbb{R}^{n_d}$ is a vector containing random values drawn independently from the standard normal distribution. For a measurement noise of 5%, corresponding to a δ value of 0.05, the measurement covariance matrix can be obtained analytically from:

$$\mathbf{R} = \delta\, \boldsymbol{\sigma}_d^2 \tag{15}$$

To perform the joint input-state estimation, a modal representation of the wind support structure is required. Fig. 5 illustrates the first three mode shapes of the modelled structure while the corresponding natural frequencies, along with a brief description, are reported in Table 3. It should be noticed at this point that higher frequencies are significantly out of the range of the frequency content of the excitation and therefore, their corresponding modes are not included in the reduced-order representation of the model. Moreover, mode shapes in the y direction are neglected due to their null contribution in the response. Finally, according to Jonkman et al. (2009), a uniform value of 1% structural damping is adopted for all modes under consideration.

Once the reduced order model is established, it is essential to investigate the identifiability and stability conditions of system inversion, as underlined by Maes et al. (2014), before the sensor configuration is determined. In order for the system to be controllable, all states should be controlled by the input or in terms of the modal characteristics, matrix $\mathbf{S}_p^T \boldsymbol{\Phi}$ should not contain zero columns. Similarly, observability of the system is ensured when all states are observable in the system output. This condition is satisfied if and only if the matrix $\mathbf{S}_d \boldsymbol{\Phi}$ does not contain zero columns.

Table 3: Natural frequencies of the FE model

No.	Frequency [Hz]	Description
1	0.290	First global lateral (fore-aft)
2	1.133	Second global lateral (fore-aft)
3	1.511	Third global lateral (fore-aft)

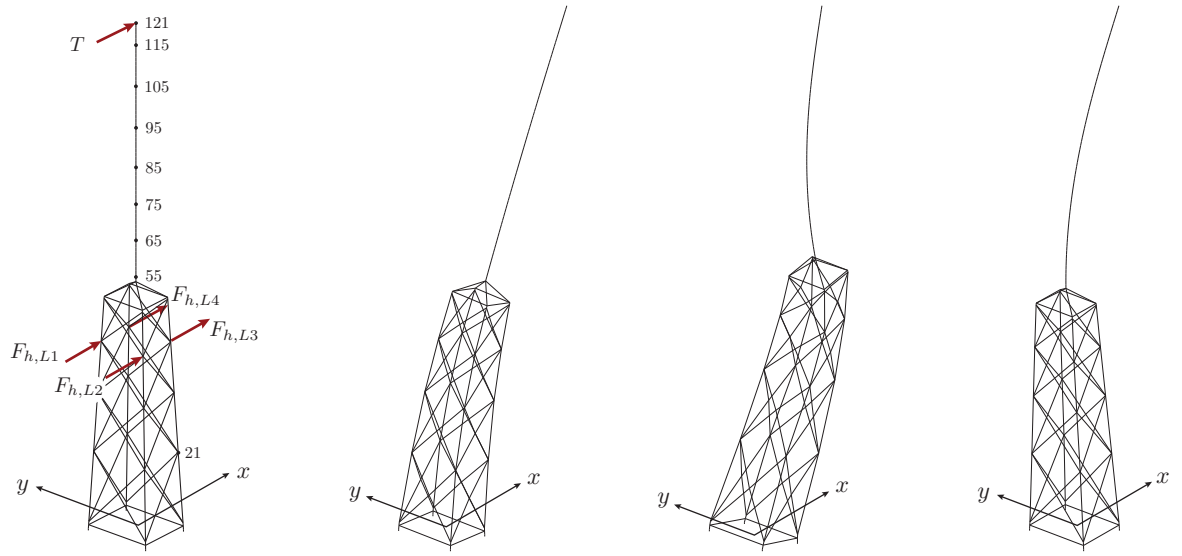

(a) FE Model (b) Mode 1 (c) Mode 2 (d) Mode 3

Figure 5: (a) Finite element model of the wind turbine support structure and (b)-(d) First three mode shapes

Finally, direct invertibility ensures that estimation of the system input can be performed without time delay. Should a modally reduced order model be used, this condition is satisfied when both the order of the model n_{m} and the number of acceleration measurements $n_{\mathrm{d,a}}$ is greater than or equal to the number of forces n_{p}, or equivalently when $\mathrm{rank}\left(\mathbf{S}_{\mathrm{p}}^{\mathrm{T}}\mathbf{\Phi}\right) = n_{\mathrm{p}}$ and $\mathrm{rank}\left(\mathbf{S}_{\mathrm{d,a}}\mathbf{\Phi}\right) \geq n_{\mathrm{p}}$ respectively. Moreover, in order to avoid unstable or marginally stable transmission zeros and ensure stability of the system inversion, the number of displacement or strain measurements $n_{\mathrm{d,d}}$ should be greater than or equal to the number of forces n_{p}.

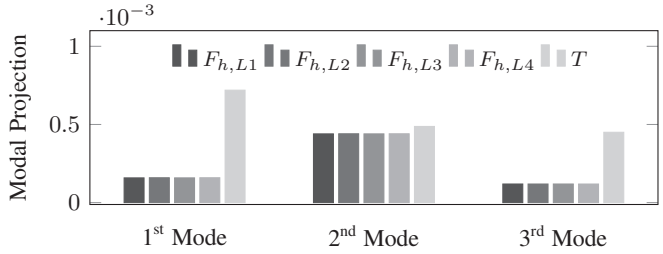

Figure 6: Graphical representation of the matrix $\mathbf{S}_{\mathrm{p}}^{\mathrm{T}}\mathbf{\Phi}$

Considering the difficulty to obtain reliable and robust measurements at locations on the jacket structure, the estimation algorithms will be based on a sensor network attached to the tower only. Figure 5(a) presents the FE model of the structure along with a set of possible sensor locations on the tower. Since state identification is aimed at, observability should be ensured and the measurement locations will be selected so as to achieve a strong coupling between observed and excited modes. A graphical representation of the matrix $\mathbf{S}_{\mathrm{d}}\mathbf{\Phi}$ is showed in Figure 7, pointing out the contribution of the modes to each one of the possible outputs. It is seen through the latter that observability may be achieved from all sensor locations under consideration.

To avoid using any a-priori information on the spatial distribution of the input, a single driving force acting at the top of the tower is identified. In so doing, it should be ensured that all states can be controlled by such an equivalent force, able to compensate for the absence of the real driving forces. From the modal projetions of the force locations $\mathbf{S}_{\mathrm{p}}^{\mathrm{T}}\mathbf{\Phi}$ as depicted in Figure (6), it is concluded that controllability of the system can be indeed achieved by the aforementioned force.

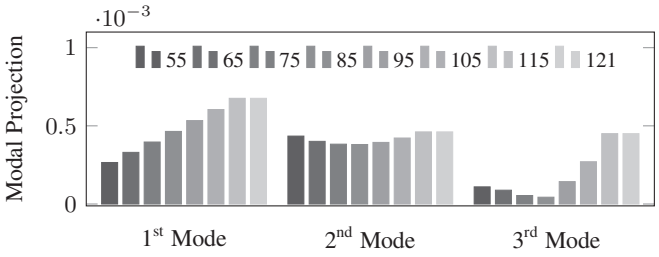

Figure 7: Graphical representation of the matrix $\mathbf{S}_{\mathrm{d}}\mathbf{\Phi}$

Dealing now with a reduced order model which comprises three mode shapes and is driven by a single input force, at least one acceleration measurement should be available in order to enable direct invertibility. Moreover, to stabilize the instantaneous system inversion, at least $n_{\mathrm{p}} = 1$ displacement or strain observations are required. Noting that the scope of this work does not encompass the optimization of the spatial distribution of the sensors and considering all the above-mentioned conditions, the sensor setup is chosen to consist of one accelerometer at the top of the tower (node 121) and a displacement sensor at node 65 (Fig. 5(a)).

5 RESULTS

In what follows, the comparative results of the two filters are presented via two distinct case studies. First, the robustness of the estimates to measurement noise is tested with an unperturbed numerical model, where process noise is absent. Next, the performance of the algorithms is assessed with an erroneous model which derives from the reference model after introduction of a certain amount of error on its natural frequencies.

The time histories of the sought-for quantities serve as the basis for the comparison study and weight is lent to the calibration of filter parameters. Moreover, particular attention is paid to the possibility of obtaining sufficiently accurate estimates for the critical underwater locations, based

on tower-only measurements. This is illustrated by means of the estimated displacement time histories of node 21 (Fig. 5(a)) which is located at the lowest K-joint of the lattice structure, 20 m above the mudline.

5.1 *Unperturbed Model*

Both filters are initialized with a zero state while the covariance matrix of the measurement noise is calculated from Eq. (15). Since no process noise is present, the initial covariance of the state $\mathbf{P}_0^{\zeta}$ and the process noise $\mathbf{Q}^{\zeta}$ are both set to $10^{-15} \times \mathbf{I}$, where $\mathbf{I}$ is an identity matrix of appropriate dimension. It should be mentioned that initialization of the GDF does not involve any information on the statistics of the input. However, the DKF requires an initial guess for the input and its covariance matrix in order to obtain the input-state estimates.

The covariance of the input is acting as a regularization parameter within the DKF algorithm and can therefore strongly affect the quality of the results. Hence, it is of crucial importance that $\mathbf{Q}^{\mathrm{p}}$ is properly adjusted to the tunning value in order for the filter to furnish accurate estimates. Within this context, use is made of the L-curve as suggested in the work of (Lourens, Reynders, De Roeck, Degrande, & Lombaert 2012). Figure 8 depicts the L-curve for the adopted sensor configuration where the horizontal axis denotes the norm of the estimation error for the measured quantities $\sum ||\mathbf{d}_k - \mathbf{G}\boldsymbol{\zeta}_k^- - \mathbf{J}\hat{\mathbf{p}}_k||_2^2/N_t$ and the vertical axis refers to the corresponding values of the covariance $\mathbf{Q}^{\mathrm{p}}$ of the input noise. It is seen that for the case of an unperturbed model the L-curve has a distinct corner at the value of $10^{11} \times \mathbf{I}$ which is assigned to the input noise covariance $\mathbf{Q}^{\mathrm{p}}$ and its initial guess $\mathbf{P}_0^{\mathrm{p}}$ accordingly.

For the given frequency content of the excitation, the structural response is dominated by the first mode shape whose estimation is therefore of particular interest. In Figure 9, the estimated time histories of the modal displacement and velocity for mode 1 are presented. It is observed that both the DKF and the GDF are able to provide sufficiently accurate estimates of the two states.

Moreover, in order to investigate to what extent the response at critical locations on the jacket structure can be estimated from the current sensor setup, the lateral displacement of node 21 (Fig. (5(a)) is calculated. Figure 10 depicts the displacement time histories estimated by the two filters. It is seen that, even with a reduced-order model consisting of only three modes, both filters deliver a satisfactory downward extrapolation of the measurement data and are able to trace the displacement time history at underwater locations. However, it is observable that the GDF can yield a better match with the target value of displacement, compared with the DKF estimates.

5.2 *Erroneous Model*

A second application of the filters is performed; this time, however, the employed model does not exactly represent the real structure. The first two natural frequencies of the numerical model are increased by 20%. Thus, the measurement data is obtained from the response of the true structure and the estimation algorithms are applied using an erroneous model whose first three natural frequencies are 0.348 Hz, 1.360 Hz and 1.511 Hz, respectively. Again,

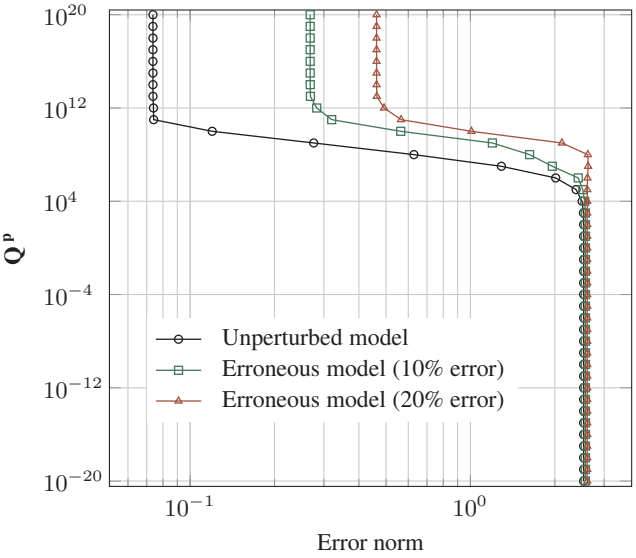

Figure 8: L-curve for the state and input identification of the wind turbine structure using DKF

5% measurement noise is introduced to the measurement data.

To initialize the procedure, a zero state is again assumed for both algorithms and the measurement noise matrix $\mathbf{R}$ is obtained by Eq. (15). In addition, the initial covariance of the state $\mathbf{P}_0^{\zeta}$ and the process noise $\mathbf{Q}^{\zeta}$ are set to $10^{-7} \times \mathbf{I}$ in order to compensate for the error introduced in the numerical model. Calibration of the input covariance $\mathbf{Q}^{\mathrm{p}}$ is also accomplished by means of the L-curve where now the curve corresponding to the erroneous model is used, as illustrated in Figure 8. It is seen that when an error is introduced in the model, the corner of the curves is becoming smoother and the tuning value is not obvious anymore. The adopted value for $\mathbf{Q}^{\mathrm{p}}$ in this case is $10^{13} \times \mathbf{I}$ which again corresponds to the lowermost point of the upper vertical segment of the L-curve.

Figure 11 shows the estimated time histories of the modal states for mode 1 when the erroneous model is used. Although there is a disagreement between the two models used for the estimation and the data generation, both algorithms can still properly trace the modal responses after proper adjustment of their parameters, with the GDF slightly ouperforming the DKF. Moreover, it is seen in Figure 12 that equally accurate estimates can be obtained for the underwater locations.

Figure 13 presents a comparison between the DKF estimates obtained with two different tuning parameters corresponding to the left and right L-curves in Figure 8. The importance of a proper tuning of $\mathbf{Q}^{\mathrm{p}}$ is apparent, as well as the dependence of this tuning on model accuracy. It should be noted here that the L-curve was developed for linear models $\mathbf{A}\mathbf{x} = \mathbf{b}$, in which only the right-hand side $\mathbf{b}$ is subjected to errors. In situations where both the coefficient matrix $\mathbf{A}$ (comparable to the state matrix $\mathbf{A}$ in a state-space setting) and the right-hand side $\mathbf{b}$ (comparable to $\mathbf{d}$ in the observation equation) contain errors, regularization methods based on Total Least Squares (TLS) should theoretically be used (Hansen 1998). The authors are of the opinion, however, that tuning difficulties will remain also with the application of more suitable regularization methods.

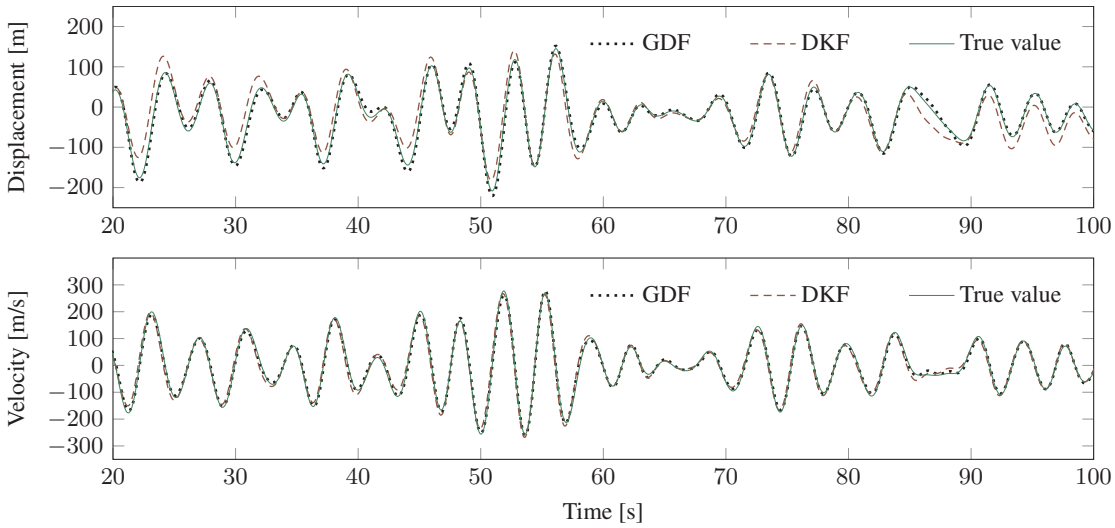

Figure 9: Modal displacement (top) and velocity (bottom) time histories estimated by GDF and DKF for mode 1 using the unperturbed model

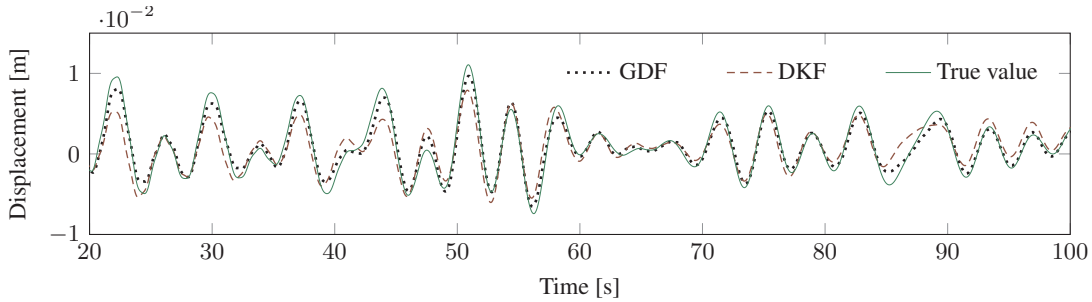

Figure 10: Displacement time histories estimated by GDF and DKF for node 21 using the unperturbed model

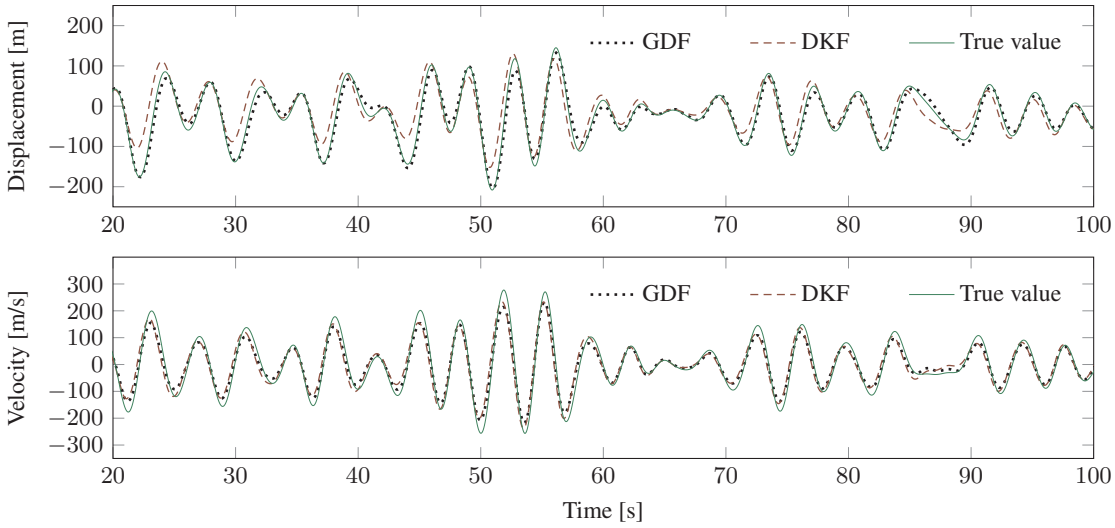

Figure 11: Modal displacement (top) and velocity (bottom) time histories estimated by GDF and DKF for mode 1 using the erroneous model

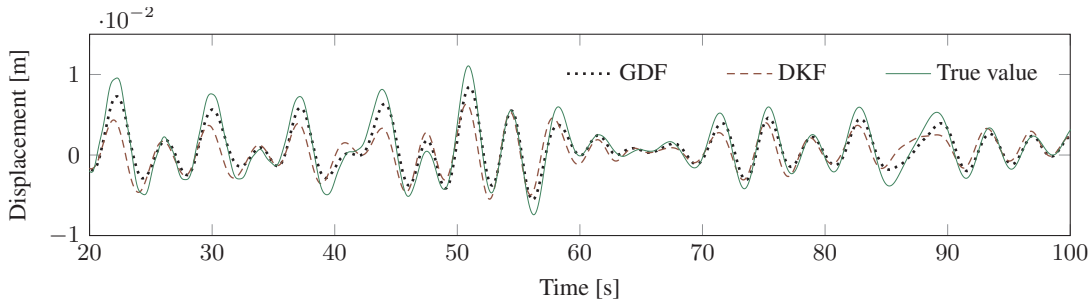

Figure 12: Displacement time histories estimated by GDF and DKF for node 21 using the erroneous model

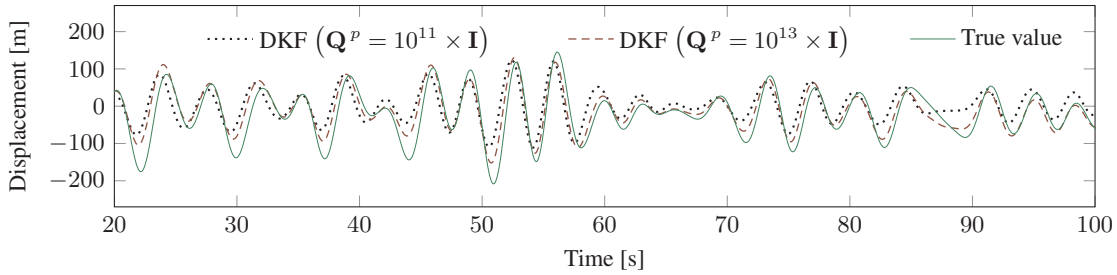

Figure 13: Modal displacement time histories estimated by DKF for mode 1 using the erroneous model; covariance $\mathbf{Q}^{\mathrm{p}}$ of input noise is tuned according to the L-curves of the unperturbed and the erroneous model at $10^{11} \times \mathbf{I}$ and $10^{13} \times \mathbf{I}$, respectively

6 CONCLUSIONS

A comparative study of two Kalman-type filters was presented, both capable of extrapolating the measured vibration response of an offshore wind turbine tower to critical locations beneath the waterline. The extrapolation is performed based on a limited set of simulated sensor data and a possible erroneous (reduced-order) model of the structure. Different analyses were performed to assess the robustness of the two filters to modelling errors and the following conclusions were drawn:

- The GDF is seen to slightly outperform the DKF where the inferiority of the DKF estimates is related to the relative difficulty in finding an optimal regularization parameter.
- A major drawback of the GDF is the fact that it requires either strain or displacement measurements for a stable estimation. Although displacement measurements are not feasible offshore, the turbine towers are, however, often equipped with strain gauges.

REFERENCES

Azam, S. E., E. Chatzi, & C. Papadimitriou (2015). A dual kalman filter approach for state estimation via output-only acceleration measurements. *Mechanical Systems and Signal Processing 60*, 866–886.

Azam, S. E., E. Chatzi, C. Papadimitriou, & A. Smyth (2015). Experimental validation of kalman-type filters for online and real-time state and input estimation. *Journal of Vibration and Control*.

Burton, T., N. Jenkins, D. Sharpe, & E. Bossanyi (2011). *Wind Energy Handbook*. West Sussex, United Kingdom: Wiley.

De Vries, W. E., N. K. Vermula, P. Passon, T. Fischer, D. Kaufer, D. Matha, B. Schmidt, & F. Vorpahl (2011). Upwind wp4 d4.2.8 final report wp4.2: Support structure concepts for deep water. Technical report, Upwind.

Gillijns, S. & B. De Moor (2007). Unbiased minimum-variance input and state estimation for linear discrete-time systems with direct feedthrough. *Automatica 43*, 934–937.

Hansen, P. C. (1998). Rank-deficient and discrete ill-posed problems. *SIAM*.

Jonkman, J., S. Butterfield, W. Musial, & G. Scott (2009). Definition of a 5-mw reference wind turbine for offshore system development. Technical report, National Renewable Energy Laboratory, Golden, Colorado.

Lourens, E., C. Papadimitriou, S. Gillijns, S. Reynders, G. de Roeck, & G. Lombaert (2012). Joint input-state estimation for structural systems based on reduced-order models and vibration data from a limited number of sensors. *Mechanical Systems and Signal Processing 29*, 310–327.

Lourens, E., E. Reynders, G. De Roeck, G. Degrande, & G. Lombaert (2012). An augmented kalman filter for force identification in structural dynamics. *Mechanical Systems and Signal Processing 27*, 446–460.

Maes, K., E. Lourens, K. van Nimmen, E. Reynders, G. de Roeck, & G. Lombaert (2014). Design of sensor networks for instantaneous inversion of modally reduced order models in structural mechanics. *Mechanical Systems and Signal Processing 52-53*, 628–644.

Shinozuka, M. & G. Deodatis (1991). Simulation of stochastic processes by spectral representation. *Applied Mechanics Reviews 44*(4), 191–204.

Van der Male, P. & E. Lourens (2015, February). Operational vibration-based response estimation for offshore wind lattice structures. *Structural Health Monitoring and Damage Detection 7*, 83–96.